Development of Geometry Optimization Methodology with In-house CFD code, and Challenge in Applying to Fuel Assembly

J. H. Jeong [a*], K. L. Lee [a]

[a] Korea Atomic Energy Research Institute, 989-111, Daedeok-daero, Yuseong-gu, Daejeon, 305-353
[*]Corresponding author: jhjeong@kaeri.re.kr

1. Introduction

The SFR (Sodium-cooled Fast Reactor) system sustains the fission chain reaction using a recycling of transuranics (TRUs) by reusing spent nuclear fuel. This situation strongly motivated the Korea Atomic Energy Research Institute (KAERI) to start a prototype Gen-IV Sodium-cooled Fast Reactor (PGSFR) design project under the national nuclear R&D program. Generally, SFR system has many different characteristics compared with other commercial nuclear reactors. Especially, the core design of SFR system has a tight package of the fuel bundle to minimize a leakage of fast neutron and it use sodium material as a coolant having a high thermal conductivity and high boiling temperature, which can make the core design to be more compact through narrower sub-channels. Therefore, the fuel assembly of PGSFR has a compact core design with 217 wire-wrapped fuel pins and a hexagonal duct, in which wire-wrapped fuel bundles has triangular loose array. The wire spacer has important roles to avoid collisions between adjacent rods, to mitigate a vortex induced vibration, and to enhance convective heat transfer by wire spacer induced secondary flow.

Many experimental and numerical works has been conducted to understand the thermal-hydraulics of the wire-wrapped fuel bundles. There has been enormous growth in computing capability. Recently, a huge increase of computer power allows to three-dimensional simulation of thermal-hydraulics of wire-wrapped fuel bundles. The applicability of RANS (Reynolds Averaged Navier-Stokes simulation) approaches has already been assessed by Pointer et al. [1]. Amad et al. [2], Gajapathy et al. [3] performed the three-dimensional flow and heat transfer analysis by using the RANS based simulation. Pointer et al. [4, 5] and Fischer et al. [6] implemented the comparison of LES and RANS results in the 7-pin fuel assembly test section. The comparison of both sub-channel mixing velocity provide some confidence that RANS based simulation can be expected to provide acceptably accurate hydrodynamic prediction.

In this study, the geometry optimization methodology with RANS based in-house CFD (Computational Fluid Dynamics) code has been successfully developed in air condition. In order to apply the developed methodology to fuel assembly, GGI (General Grid Interface) function is developed for in-house CFD code. Furthermore, three-dimensional flow fields calculated with in-house CFD code are compared with those calculated with general purpose commercial CFD solver, CFX.

2. Numerical Design Methodology Development

Geometry optimization methods are generally classified into two categories: inverse design and direct design. For implementing the inverse design, designer should have knowledge and experience of how to distribute velocity or pressure on a certain shape surface in order to obtain desirable aerodynamic characteristics. An alternative to the inverse design is offered by the direct design using numerical optimization such as a GA (Genetic Algorithm) and RSM (Response Surface Methodology) and so on. Any knowledge and experience of geometry optimization are not required as using the direct design. In this study, geometry optimization with the GA and in-house CFD code is developed using the simple airfoil shape which has high thickness ratio, because they generate complicated separation vortex on the upper surface around trailing edge.

2.1 Design Algorithm

Holland in 1975 has begun to propose the optimization process, called a GA which simulates the process of evolution in nature of organisms. The organisms produce a number of individuals in each generation. The individuals adapted to the environment better have higher chance to survive. Selected individuals have a chance to produce a number of individuals similar to themselves for next generation through their choromo-somes by a process of called crossover. Some of individuals can have variation due to mutation in order to find the global optimum solution without becoming trapped at local optima. [7, 8]

Figure 1 shows the direct design flow chart of airfoil shape optimization with the GA and in-house CFD code. As shown in Fig. 1, the direct design is carried out by means of an iterative numerical calculation to maximize fitness value while satisfying the constraint condition. For evaluating fitness value of complex shape which is dominated by separated and vortical flow, high-accuracy CFD analysis based on the RANS equations is carried out on all population of each generation. In this study, the direct design is conducted by means of an iterative numerical optimization to maximize objective function. The X and Y coordinates of each shape correspond to the choromo-somes of each individual. In

the first stage of optimization, aerodynamic characteristic of the baseline shape is evaluated by the CFD analysis. Initial population (1st generation) of 20 shapes that have different X and Y coordinates is randomly generated while satisfying the constraint conditions.
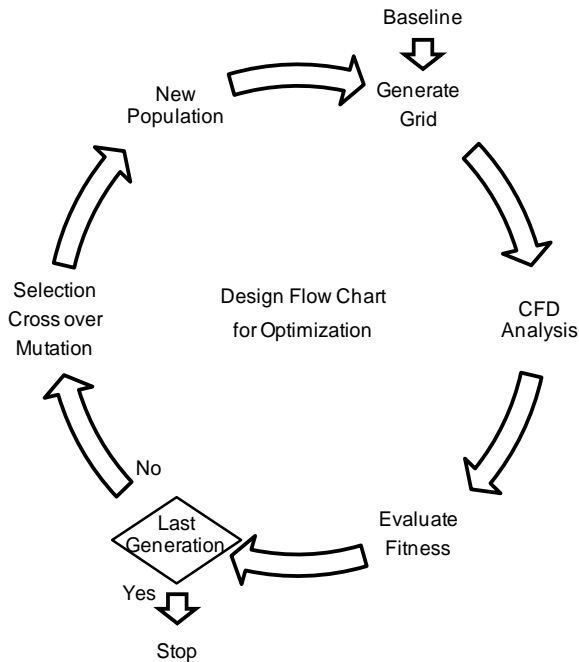

Fig. 1. Direct design flow chart of geometry optimization with GA and in-house CFD code

As implementing grid generation and CFD analysis of each airfoil shape, the object unction is evaluated by the CFD analysis results. A lift and drag coefficient of CFD analysis are calculated by integration of pressure and shear stress around the airfoil surface. The selection according to the objective function plays an important role in driving the search towards better airfoils which have higher lift to drag ratio and maintain initial lift coefficient. For sharing X and Y coordinates between two successful airfoils, the crossover is implemented. A few of X and Y coordinates are randomly chosen to conduct the mutation. Through the selection, crossover, and mutation, new population (2nd generation) of 20 airfoils are created. The design parameters, objective function, constraints, and the number of individuals and generations in this study are as the following.

■ *Find*

$X = \quad x_1, y_1 \quad , \quad x_2, y_2 \quad ,..., \quad x_{19}, y_{19}$

$x_1, y_1 \quad = \quad x_{19}, y_{19} \quad = (1, 0)$

$x_{10}, y_{10} \quad = (0, 0)$

■ *Maximize*

$F(X) = \dfrac{lift\_coefficient}{drag\_coefficient}$

$where, lift\_coefficient(X) \geq Initial\_lift\_cofficient$

■ *Subject to*

$C(X) \geq Airfoil\_thickness$

■ *The number of individuals*

$Individuals = 20$

■ *The number of generations*

$Generations = 10$

2.2 Test Shape for Optimization with GA and CFD

An airfoil shape can be determined by many spline methods such as B-spline, Bezier, Akima and so on. Each spline's characteristics are as follows. B-spline is a spline with a soft curve that runs between, but through, the vertices. Bezier is a spline with a soft curve that runs through and between the vertices, but with moderated cornering that can be precisely adjusted by tangent control points. Akima is a spline with a soft curve that runs through and between the vertices, but with tight cornering [9]. In this study, the Akima curve fitting method was adapted to generate the airfoil shape in order to take into account locally tight cornering of leading edge and trailing edge and to minimize over-shooting or over-fitting problem [10]. Figure 2 shows the control points of airfoil geometry. As shown in Fig. 1 and 2, the 19 X and Y coordinates are one of the most important design parameters in the optimization system.
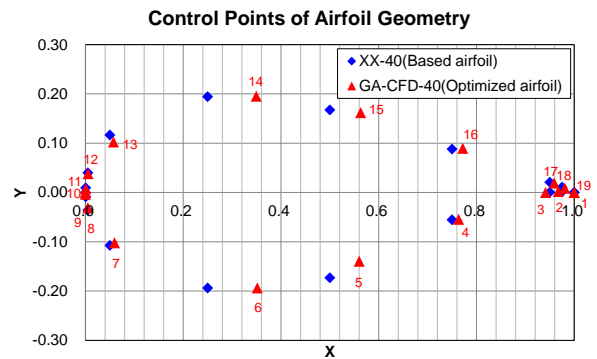

Fig. 2. Control points of airfoil geometry (diamond marking with blue color: baseline airfoil, triangle marking with red color: optimized airfoil)

There are two kinds of general grid generation system with C and O type, which are suitable for the airfoils with sharp trailing edge and blunt trailing edge, respectively. As the optimization of this study is carried out for the airfoil with sharp trailing edge, C type grid generation system is selected for minimizing cell skewness.

Figure 3 shows the C type computational grid system of the baseline airfoil. As shown in Fig. 3, a far-field distance from the airfoil surface is 10 times of chord length. Block 1, 2, and 3 represent suction surface region, pressure surface region, and outflow region, respectively. The computational cells of Fig. 3 are concentrated around the airfoil surface was latticed more than half of all cells, because this region is the most important field to understand a complicated and

vortical flow in the airfoil. Furthermore, the minimum spacing of airfoil surface is approximately 1.0×10^{-5} that is almost same that Y^+ is 1 at Reynolds number with 1.5×10^6. The *k-w* turbulence model utilized in CFD analysis works best with an initial spacing that is Y^+ under 1[11]. The number of cells on block 1, 2, and 3 is 1.0×10^4.
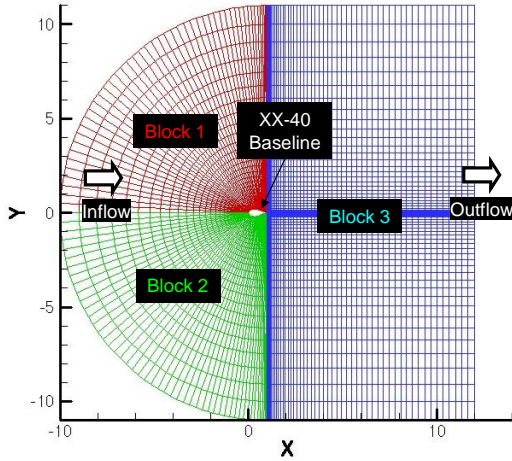
(a) Overall view of computational grid system
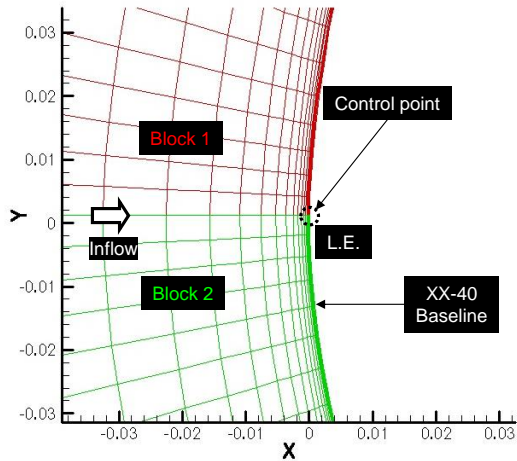
(b) Enlarged view of airfoil leading edge
Fig. 3. Computational grid system

2.3 Numerical Method of In-house Code

In recent years, many numerical schemes for the Navier-Stokes simulation have been developed. To evaluate aerodynamic characteristics of each airfoil, three-dimensional Reynolds-averaged Navier-Stokes (RANS) equations were solved by an implicit upwind relaxation scheme [12]. Compressible Navier-Stokes equations were discretized in space using a cell-centered finite volume formulation. The two-dimensional, Reynolds-averaged Navier-Stokes equations are integrated over a computational cell. The integrated equations can be written in non-dimensional form as

$$\frac{\partial}{\partial t} \int_\Omega Q d\Omega + \int_\Omega H dS = \frac{1}{\mathrm{Re}} \int_\Omega R dS \qquad (1)$$

where the cell region is denoted by Ω, the cell boundary by $\partial\Omega$, and the distance along the boundary by *S*. In the above, Re denotes the Reynolds number, and *Q*, *H*, and *R* are the vectors of conserved variables, inviscid fluxes and viscous fluxes, respectively, which are given by

$$Q = \begin{bmatrix} \rho \\ \rho u \\ \rho v \\ e \end{bmatrix}, H = \begin{bmatrix} \rho U \\ \rho u U + p n_x \\ \rho u U + p n_y \\ e + p \; U \end{bmatrix}, R = \begin{bmatrix} 0 \\ \tau_{xx} n_x + \tau_{xy} n_y \\ \tau_{xy} n_x + \tau_{yy} n_y \\ f_x n_x + f_y n_y \end{bmatrix} \qquad (2)$$

with

$$U = u n_x + v n_y$$
$$\tau_{xx} = \mu \; 4u_x - 2v_y \; /3$$
$$\tau_{xy} = \mu \; u_y + v_x$$
$$\tau_{yy} = \mu \; 4v_y - 2u_x \; /3$$
$$f_x = \mu\tau_{xx} + v\tau_{xy} + \; \mu/\mathrm{Pr} \; \gamma - 1^{-1} \; a^2 \;_x$$
$$f_y = \mu\tau_{xy} + v\tau_{yy} + \; \mu/\mathrm{Pr} \; \gamma - 1^{-1} \; a^2 \;_y$$

Here, ρ is the density, *u* and *v* are the velocity components in the *x* and *y* directions, respectively, *e* is the total energy per unit volume, *p* is the pressure, n_x and n_y are the *x* and *y* components of the outward unit vector normal to the cell boundary, γ is the ratio of specific heats, and a is the speed of sound. In addition, μ and μ/Pr are expressed as follows using the molecular viscosity μ_l given by the Sutherland's law, the eddy viscosity μ_t, the laminar Prandtl number Pr_l, and the turbulent Prandtl number Pr_t :

$$\mu = \mu_l + \mu_t \qquad (3)$$
$$\mu/\mathrm{Pr} = \mu_l/\mathrm{Pr}_l + \mu_t/\mathrm{Pr}_t$$

In the present scheme, the Prandtl numbers, Pr_l and Pr_t, are assumed to be constant. Only the perfect gas will be considered, in which case the pressure and speed of sound can be given by

$$p = \; \gamma - 1 \; e - p \; u^2 + v^2 \; /2 \qquad (4)$$
$$a = \gamma \; \gamma - 1 \; e/\rho - \; u^2 + v^2 \; /2$$

All the variables in the above equations are non-dimensionalized with the density, speed of sound, molecular viscosity in the upstream, and a reference length taken as the representative length.

The inviscid flux were evaluated by high-resolution upwind scheme based on a TVD (Total Variation Diminishing) formulation [13] where a Roe's approximate Riemann solver of Chakravarthy [14] and a third-order accurate MUSCL approach of Anderson et al. [15] with the Van Albada limiter [16] were

implemented. The high-resolution upwind schemes generally have non-oscillatory but sharp shock capturing properties without any tuning of the artificial dissipation terms. The viscous fluxes were determined in a central differencing manner with Gauss's theorem. Equations linearized in time were solved simultaneously by a point Gauss-Seidel relaxation method using no approximate factorization. And the eddy viscosity is estimated by the *k-w* turbulence model [11] performs significantly well under adverse pressure gradient condition around the suction surface of the airfoil trailing edge. In this study, above flow solver is called as in-house CFD code.

2.4 Evaluation Condition

Evaluation conditions of the airfoil optimization are as below. Table 1 shows the evaluation condition details.

Table 1. Evaluation condition details

Analysis conditions	Value
Reynold number	1.5×10^6
Angle of attack (deg)	10
Aerodynamic roughness	5 (smooth)
Airfoil surface boundary condition	No slip
Periodic boundary condition	Symmetric
Inlet and outlet boundary condition	Free stream

2.5 In-house CFD code validation

Optimization with the GA is fully dependent on the evaluation results of the flow solver. In this reason, validation of the in-house CFD code was conducted by comparison of CFD analysis results with experimental results of the airfoil (NACA4412). Figure 4 shows the pressure coefficient of NACA4412 at 13.87 deg of AOA (Angle Of Attack) and 1.52×10^6 Reynolds
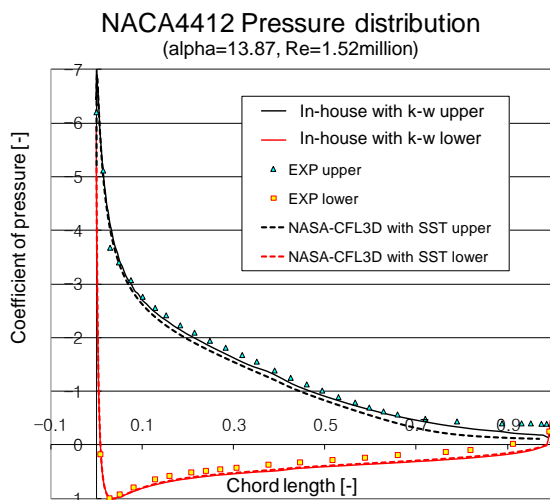

Fig. 4. Pressure coefficient distribution of NACA4412 (AOA=13.87 deg, Re=1.52×10^6)

number that are similar to evaluation condition of this study. As shown in Fig. 4, pressure coefficient of the in-house CFD code is in good agreement with the experimental results and NASA-CFL3D analysis results.

2.6 Optimization results of 35% and 40 % thick airfoil

Figure 5 shows the objective function history of 35% and 40% thickness airfoil, respectively. In terms of 35% thickness airfoil, the lift to drag ratio of baseline and optimized airfoil is from 13.33 to 19.03. In case of 40% thickness airfoil, the lift to drag ratio of baseline and optimized airfoil is from 10.77 to 13.76. The geometry optimization of 35% and 40% thickness achieves aerodynamic performance improvement by as much as 42.8% and 27.8%, respectively. Table 2 and 3 show the aerodynamic characteristics of the baseline and optimized airfoils with 35% and 40% thickness at optimization condition, respectively.
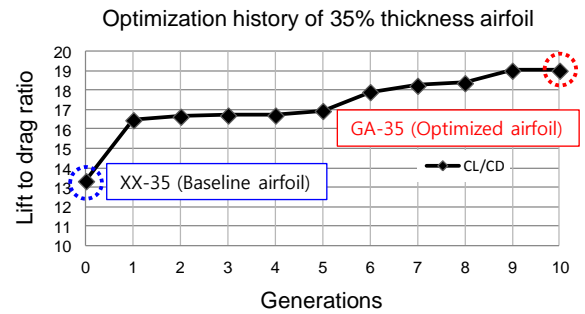
(a) 35% thick airfoil
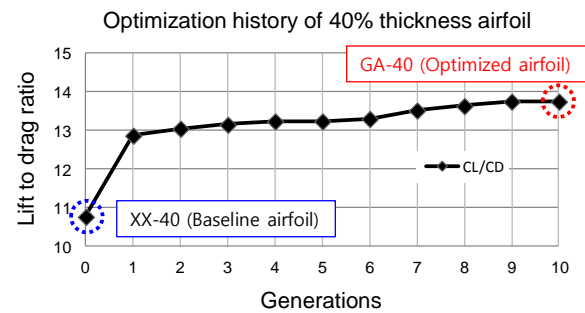
(b) 40% thick airfoil

Fig. 5. Objective function history of baseline and optimized airfoils

Table 2. Aerodynamic characteristics of 35% thick airfoil baseline and optimized airfoils

Calculated parameters	Baseline	Optimized
Lift coefficient	1.448	1.456
Drag coefficient	0.1086	0.0765
Lift to drag ratio	13.33	19.03
Bending coefficient	-0.1690	-0.1725

Table 3. Aerodynamic characteristics of 40% thick airfoil baseline and optimized airfoils

Calculated parameters	Baseline	Optimized
Lift coefficient	1.231	1.275
Drag coefficient	0.1144	0.0927
Lift to drag ratio	10.77	13.76
Bending coefficient	-0.1319	-0.1343

Figure 6 shows the velocity magnitude distribution normalized by sound velocity and streamline of 35% and 40% thickness airfoils. As shown in Fig. 6, vortical flow fields around the upper trailing edge region are dominated by separation vortex structure which is generated by adverse pressure gradient. Separation vortex in left side of baseline airfoils is larger than that in right side of optimized airfoils. It is expected that control of separation vortex would be effective on reduction of the drag coefficient.
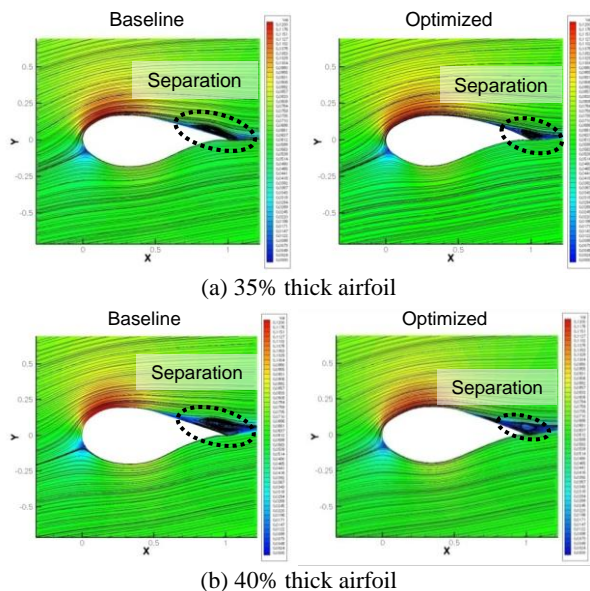

(a) 35% thick airfoil

(b) 40% thick airfoil

Fig. 6. Velocity magnitude distribution and streamline of 35% and 40% thick airfoils (left: baseline airfoils, right: optimized airfoils)

3. Challenge in Applying to Fuel Assembly

As mentioned previously, the geometry optimization methodology has been successfully developed based on the GA and in-house CFD code. Raza et al. has tried to optimize wire-wrapped fuel assembly shape Kriging metamodeling technique [17]. In this chapter, in order to apply the developed methodology to fuel assembly, GGI (General Grid Interface) function is developed for in-house CFD code. Furthermore, three-dimensional flow fields calculated with in-house CFD code are compared with those calculated with general purpose commercial CFD solver, CFX.

3.1 Test Section of Numerical Analysis

A numerical analysis methodology applied to arbitrarily assumed 1-pin fuel assembly. The arbitrarily assumed geometric parameters of the 1-pin fuel assembly are summarized in Table 4.

Figure 7 shows a schematic of the test section and a cross sectional view of the fuel assembly with wire spacer. As shown in Table 4 and Fig. 7, a 1-pin bundle was centered in a hexagonal duct, with 11.26 mm flat-to-flat distance inside. The pin was 8.5 mm in diameter, wrapped by wire spacers of 1.1 mm in diameter with a wrapping lead of 200 mm. The pitch-to-diameter ratio (P/D) was 1.135.

Table 4. Test section geometric parameters of 1-pin with wire

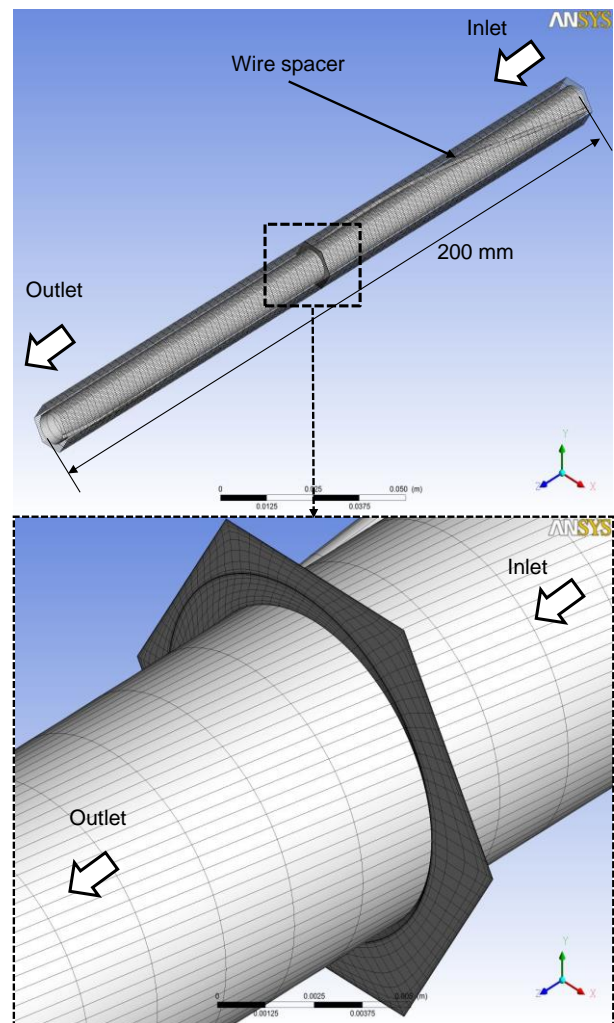| Geometric parameters	Value
Number of pins	1
Pin diameter (mm)	8.5
Pin pitch (mm)	9.65
Pitch to pin diameter ratio	1.135
Pin length (mm)	200
Duct inner flat-to-flat distance (mm)	11.26
Wire spacer diameter (mm)	1.1
Wire lead pitch (mm)	200

Fig. 7. Schematic of the test section

3.2 Computational Grids and Boundary Conditions

Figure 8 shows the cross sectional view with mesh distribution, which is divided into inner fluid region and outer fluid region. This computational grid system of fuel assembly is proposed by Jeong et al. [18]. They have presented a possible path for the RANS based CFD methodology with innovative grid generation, which is applicable to real scale 217-pin wire-wrapped fuel assembly of KAERI PGSFR. As shown in Fig. 8, in the innovative grid generation using in-house grid generation code, the boundary line (red dotted line) between the helically arranged meshes (inner fluid region) and straightly arranged meshes (outer fluid region) is adopted with General Grid Interface (GGI) function that can couple different meshes.
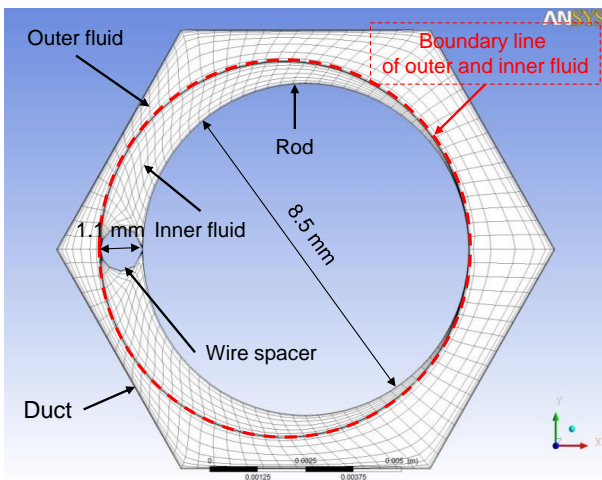

Fig. 8. Cross sectional view with grid distribution

Table 5 describes the computational grids system. The computational grid system is divided into two regions: an inner fluid part and outer fluid part. Both inner and outer fluid volume is filled with hexahedral meshes. The total number of computational grids in the system was approx. 1.87×10^5 cells.

Table 5. Computational grid system

1-Pin	Cells	Nodes	Elements
Inner fluid	86,400	94,210	86,400
Outer fluid	100,800	109,910	100,800
Total	187,200	204,120	187,200

Table 6 describes the computational boundary condition of the CFD analysis. The inlet and outlet are defined with various velocities, a temperature of 298.15 K, and a relative pressure of atmospheric pressure, respectively. The surfaces of the rod, wire spacer, and duct wall are defined with no slip condition, conservative interface flux, and smooth roughness.

Table 6. Boundary condition in the 1-pin fuel assembly

Boundary domain	Condition	Value
-Inlet	-Constant velocity [m/s]	15
-Outlet	-Relative pressure [Pa]	Atmospheric pressure
-Rod -Wire spacer -Duct wall	-No slip (Adiabatic Smooth wall)	-

3.3 Turbulence Model

Three major numerical analysis techniques can be used for turbulent flow fields: DNS (Direct Numerical Simulation),

LES (Large Eddy Simulation), and RANS (Reynolds-averaged Navier-Stokes) simulation. In order to precisely analyze the general vortex behavior in a turbulent flow field containing vortices of various scales, it is necessary to make the calculation grid size smaller than the minimum space scale of the vortex structure and the time interval less than the minimum time scale of the vortex variation. Assuming that computing the cost of the RANS is equal to one, that of the DNS and LES increases as the cube and square of the Reynolds number, respectively. The Reynolds number based on the averaged axial velocity and the hydraulic diameter of the present fuel assembly is higher than 1.29×10^4. For this reason, the DNS and LES are not feasible methods. RANS is a very practical and affordable engineering solution with good knowledge of the turbulence.

In the present study, we conducted the steady RANS simulation with the *k-w* turbulence model [8] for comparing the three-dimensional and vortical flow structures between CFX and in-house CFD code. The high-resolution scheme was used in both CFD analyses. Convergence of the simulation was judged by the periodic mass flowrate and maximum residual value.
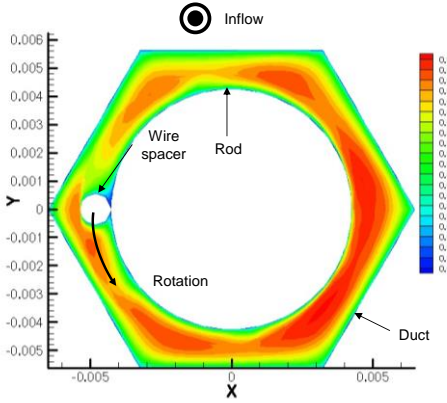
3.4 Comparison of CFX Results with In-house CFD Code results

Figs. 9, 10, 11, 12, and 13 show the comparison of normalized velocity magnitude distribution, velocity distribution in X, Y, and Z direction, and streamline with CFX and in-house code on the cross-sectional plane of fuel assembly. As shown in Figs., normalized velocity distributions and streamline results with CFX and in-house code are very close to each other.

Peak velocity and Z-velocity positions in Figs. 9 and 12 are located at almost same region. In-house CFD code can sharply capture the flow phenomena on the cross sectional plane than CFX. Narrow sub-channel has lower velocity than wide sub-channel because of geometric resistances. Even though both analyses are conducted with same computation grid system,
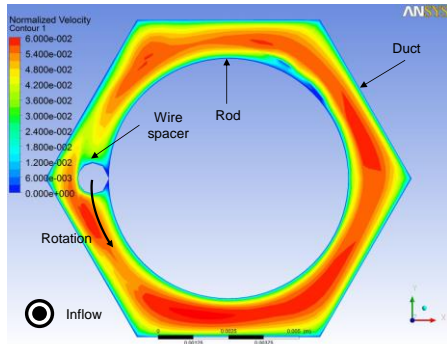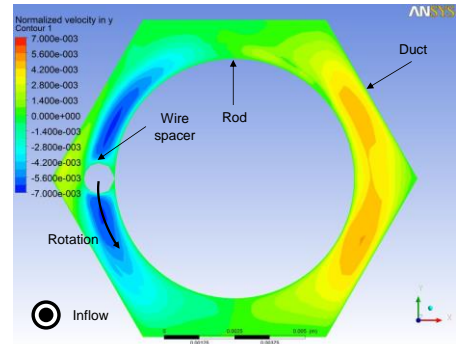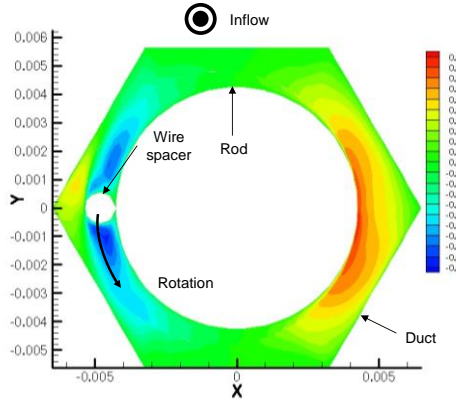
(a) CFD results with CFX

(b) CFD results with in-house code

Fig. 9. Comparison of normalized velocity magnitude distribution with CFX and in-house code on the cross-sectional plane of fuel assembly
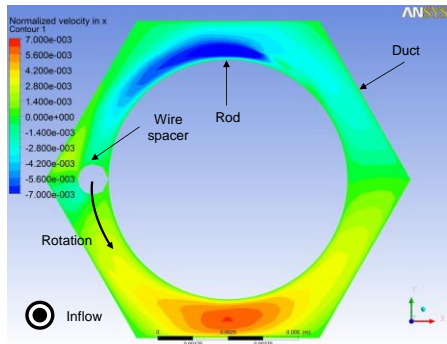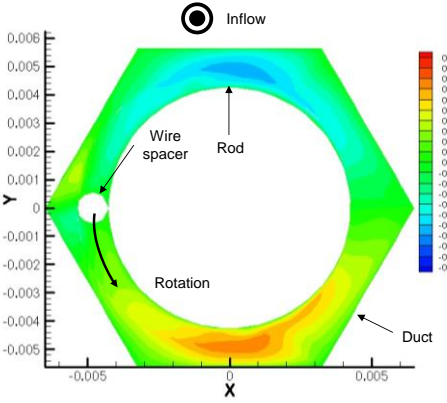

(a) CFD results with CFX

(b) CFD results with in-house code

Fig. 10. Comparison of normalized velocity distribution in X direction with CFX and in-house code on the cross-sectional plane of fuel assembly

(a) CFD results with CFX

(b) CFD results with in-house code

Fig. 11. Comparison of normalized velocity distribution in Y direction with CFX and in-house code on the cross-sectional plane of fuel assembly
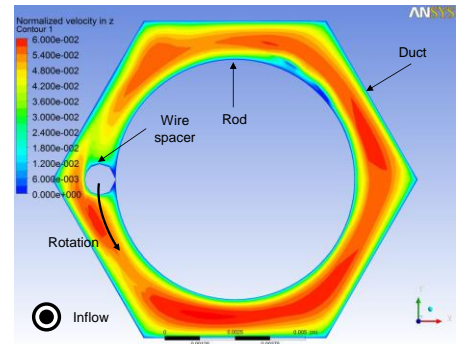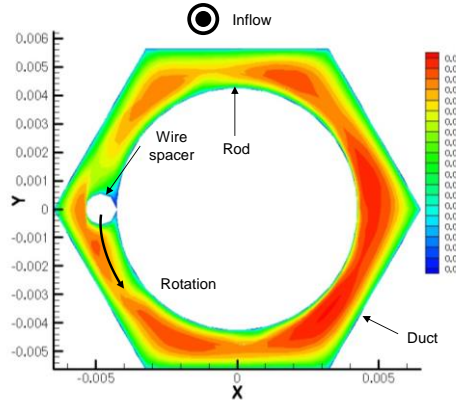

(a) CFD results with CFX

(b) CFD results with in-house code

Fig. 12. Comparison of normalized velocity distribution in Z direction with CFX and in-house code on the cross-sectional plane of fuel assembly

(a) CFD results with CFX
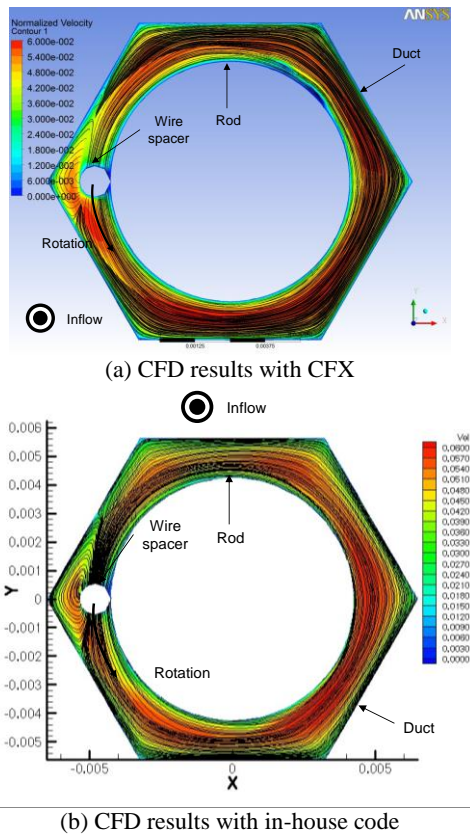

(b) CFD results with in-house code

Fig. 13. Comparison of streamline and normalized velocity magnitude distribution with CFX and in-house code on the cross-sectional plane of fuel assembly

numerical error of GGI function in CFX locally occurred around rod surface and boundary region between inner fluid and outer fluid region. In this reason, CFD analysis results with CFX seem to have blockage effects due to vortex structure around rod surface.

Peak X and Y velocity positions in Figs. 10 and 11 are located at different position with different velocity magnitude. Based on the Figs. 10 and 11, tangential velocity calculated by CFX in the X and Y direction is 15% higher than that calculated by in-house CFD code. These differences between CFX and in-house CFD code should be elucidated by comparison with experimental data in further study.

4. Conclusions

The geometry optimization methodology with RANS based in-house CFD code has been successfully developed in air condition. In order to apply the developed methodology to fuel assembly, GGI function is developed for in-house CFD code as same as CFX. Furthermore, three-dimensional flow fields calculated with in-house CFD code are compared with those calculated with general purpose commercial CFD solver, CFX.

Peak Z velocity positions and streamline distribution on the cross sectional plane between CFX and in-house code are very close to each analysis result. However, Peak X and Y velocity positions on the cross sectional plane between CFX and in-house code positions are located at different regions, and they have different level of X and Y velocity. Furthermore, even though both analyses are conducted with same computational meshes, numerical error due to GGI function locally occurred in only CFX solver around rod surface and boundary region between inner fluid region and outer fluid region.

REFERENCES

[1] W.D. Pointer, P. Fischer, A. Siegel, and J. Smith, RANS-based CFD simulations of wire-wrapped fast reactor fuel assemblies, *Proceedings of ICAPP '08*, Anaheim, California, 2008.
[2] I. Ahmad, K.Y. Kim, Flow and convective heat transfer analysis using RANS for a wire-wrapped fuel assembly, *Journal of Mechanical Science and Technology*, 20, 1514-1524, 2006.
[3] R. Gajapathy, K. velusamy, P. Selvaraj, P. Chellapandi, and S.C. Chetal, CFD investigation of helical wire-wrapped 7-pin fuel bundle and the challenges in modeling full scale 217 pin bundle, *Nuclear Engineering and Design*, 237, 2332-2342, 2007.
[4] W.D. Pointer, J.T. Tom, T. Fanning, P. Fischer, A. Siegel, J. Smith, and A. Tokuhiro, RANS-based CFD simulation of sodium fast reactor wire-wrapped pin bundles, Proceedings of International Conference on Mathematics, Computational Methods & Physics (M&C 2009), Saratoga Springs, New York.
[5] W.D. Pointer, P. Fischer, J. Smith, A. Obabko, and A. Siegel, Simulations of turbulent diffusion in wire-wrapped sodium fast reactor fuel assembly, Proceedings of International Conference on Fast Reactors and Associated Fuel Cycle, Kyoto, Japan, 2009.
[6] P.F. Fischer, A. Siegel, and P. Palmiotti, Large eddy simulation of wire wrapped fuel pins Ⅰ: Hydrodynamics in a periodic array, Proceedings of International Conference on Mathematics, Computational Methods & Physics (M&C 2007), Monterey, California.
[7] J. H. Holland, Adaptation in natural and artificial systems, Ann Arbor, *MI: University of Michigan Press*, 1975.
[8] D. E. Goldberg, Genetic algorithms in search, optimization, and machine learning, *Reading, MA: Addison-Wesley*, 1989.
[9] Modeling with splines and NURBS, GCC: Art Department, http://art.g.mass.edu/files/art268/splines_nurbs.pdf
[10] H. Akima, A new method of interpolation and smooth curve fitting based on local procedures, *J. Assoc. Comput.*, pp. 589-602, 1970.
[11] D. C. Wilcox, Reassessment of the scale-determining equation for advanced turbulence models, *AIAA Journal*, Vol. 26, No. 11, pp. 1299-1310, 1988.
[12] M. Furukawa et al., Unsteady Navier-Stokes simulation of transonic cascade flow using an unfactored implicit upwind relaxation scheme with inner iterations, *ASME Journal of Turbomachinery*, Vol. 114, No. 3, pp. 599-606, 1992.

[13] M. Furukawa et al., A zonal approach for Navier-Stokes computations of compressible cascade flow fields using a TVD finite volume method, *ASME Journal of Turbomachinery*, Vol. 113, No. 4, pp. 573-582, 1991.

[14] S. R. Chakravarthy, Relaxation method for unfactored implicit upwind schemes, *AIAA Paper*, No. 84-0165, 1984.

[15] W. Anderson et al., Comparison of finite volume flux vector splitting for the Euler equations, *AIAA Journal*, Vol. 24, No. 9, pp. 1453-1460, 1986.

[16] G. D. Van Alvada et al., A comparative study of computational methods in cosmic gas dynamics, *Aston. Astrophysics*, Vol. 108, pp. 76-84, 1982.

[17] W. Raza, K.Y. Kim, Shape optimization of wire-wrapped fuel assembly using Kriging metamodeling technique, *Nuclear Engineering and Design*, 238, pp. 1332-1341, 2008.

[18] J. H. Jeong et al., RANS based CFD methodology and challenge in modeling real scale 217-pin wire-wrapped fuel assembly of KAERI PGSFR, *The 23rd International Conference on Nuclear Engineering*, Chiba, Japan, ICONE23-1331, 2015.